Title
Investigation of the modes of NO adsorption in Pd/H-CHA

Authors
Kim, Paul
Van der Mynsbrugge, Jeroen
Aljama, Hassan
et al.

Publication Date
2022-05-01

DOI
10.1016/j.apcatb.2021.120992

Peer reviewed

Applied Catalysis B: Environmental 304 (2022) 120992

Contents lists available at ScienceDirect

Applied Catalysis B: Environmental

journal homepage: www.elsevier.com/locate/apcatb

Investigation of the modes of NO adsorption in Pd/H-CHA

Paul Kim [a,1], Jeroen Van der Mynsbrugge [a,1], Hassan Aljama [a], Trevor M. Lardinois [b], Rajamani Gounder [b], Martin Head-Gordon [c,d], Alexis T. Bell [a,d,*]

[a] Department of Chemical and Biomolecular Engineering, University of California, Berkeley, CA 94720, USA
[b] Davidson School of Chemical Engineering, Purdue University, West Lafayette, IN 47907, USA
[c] Department of Chemistry, University of California, Berkeley, CA 94720, USA
[d] Chemical Sciences Division, Lawrence Berkeley National Laboratory, Berkeley, CA 94720, USA

ARTICLE INFO

Keywords:
Passive NO_x adsorption
Zeolites
IR spectroscopy
QM/MM

ABSTRACT

This study investigates NO adsorption on Pd-exchanged chabazite (Pd/H-CHA), a promising passive NO_x adsorber (PNA) for capturing cold-start NO_x emissions of gasoline- and diesel-powered vehicles. Temperature-programed desorption (TPD) and IR spectroscopy are combined with theoretical calculations to elucidate how and where NO is stored, and how water and O_2 affect this process. NO adsorption on Pd/H-CHA produces two TPD features, around 423 and 753 K, and IR bands centered at 1860 and 1810 cm^{-1}. Calculated NO stretching frequencies and maximum-desorption temperatures reveal that Pd^{2+} and Pd^{+} sites are responsible for these low- and high-temperature features, respectively, and that while the IR feature at 1810 cm^{-1} is due to NO adsorption on Pd^{+}, the 1860 cm^{-1} feature contains contributions from both weakly-bound NO on Pd^{2+} and more strongly bound NO on Pd^{+}, consistent with experimentally observed effects of water and O_2.

1. Introduction

A particularly effective strategy for dealing with vehicular exhaust has been the three-way catalytic convertor. First installed in 1972, it has led to orders of magnitude reductions in tailpipe emissions of CO, hydrocarbons (HC), and nitrogen oxides NO_x (x = 1,2). However, a remaining challenge in emissions control using catalytic converters is the time required to reach efficient operating temperatures (>473 K) [1]. During this period, called the cold-start, the catalyst is not sufficiently active, and pollutants escape into the air unconverted. Consequently, under Tier 3 regulations of the US Environmental Protection Agency, automobiles will need to take additional steps to minimize the amount of NO_x and HC emitted during cold-start [2].

One way to reduce NO_x emissions during cold-start is to adsorb NO together with CO and unburned hydrocarbons, and then to desorb these gases so that NO can be reduced in the catalytic converter once it reaches a temperature of 523–573 K. This can be done using a passive NO_x adsorber (PNA), a device placed upstream of the catalytic converter that adsorbs NO_x emissions while the converter is heating up [3]. The PNA consists of a metal dispersed on a high surface area support, such as a zeolite or mixed oxide [4]. Pd has been identified as a particularly attractive adsorbent for PNAs because of its high capacity for NO_x storage as molecular NO or as intermediates such as nitrites [5–7]. Because of its hydrothermal stability (stable up 1023 K for up to 16 h in air and water), the zeolite chabazite (CHA) has been identified as the most suitable support for Pd [8–10].

Several investigators have reported that the manner of Pd introduction onto a zeolite support and the subsequent pretreatment and usage conditions affect the NO storage capacity and release temperature of the PNA material [11–13]. These studies and others have also shown that Pd can be present in multiple forms: isolated Pd cations (Pd^{2+}, $Pd(OH)^{+}$, Pd^{+}), PdO_x (x = 1,2) nanoparticles, and metallic Pd nanoparticles [14–19]. IR studies indicate that NO does not adsorb on PdO_x nanoparticles and adsorbs only weakly on metallic Pd nanoparticles.[17, 20,21]. Therefore, isolated Pd cations are desired for PNAs, and the loss of such centers leads to a loss in the low-temperature NO adsorption capacity of the PNA [12].

The critical role that isolated Pd cations have on NO adsorption is supported by recent work on Pd/H-CHA samples prepared to have Pd present predominantly as isolated Pd cations [15]. IR spectra of adsorbed NO showed bands at 2170 cm^{-1}, 1865 cm^{-1}, and 1805 cm^{-1}, which were assigned to $NO^{+}Z^{-}$, (NO) $Pd^{2+}(Z^{-})_2$, and (NO) $Pd^{+}Z^{-}$, respectively,

* Corresponding author at: Department of Chemical and Biomolecular Engineering, University of California, Berkeley, CA 94720, USA.
E-mail address: alexbell@berkeley.edu (A.T. Bell).
[1] Contributed equally

https://doi.org/10.1016/j.apcatb.2021.120992
Received 20 July 2021; Received in revised form 13 November 2021; Accepted 1 December 2021
Available online 6 December 2021

with the aid of DFT calculations [15,22,23] (Z^- denotes a cation-exchange site in the zeolite framework created by the isomorphous substitution of tetravalent Si with trivalent Al). The presence of Pd^{2+} in as-prepared Pd/H-CHA samples has been supported by X-ray photoelectron spectroscopy, X-ray absorption spectroscopy, and diffuse reflectance UV–vis spectroscopy [24]. Pd^+ cations have been suggested to be produced upon NO adsorption via the reaction of $Pd^{2+}(Z^-)_2 + 2\ NO \rightarrow (NO)\ Pd^+\ Z^- + NO^+Z^-$, based on the appearance of IR bands at 1805 cm^{-1} and 2160 cm^{-1} [15], and as discussed below, recent density functional theory (DFT) calculations that indicate that Pd/H-CHA treated in water vapor at high temperatures should thermodynamically favor the presence of Pd^+ cations. DFT calculations using the GGA functional PW91-D2 by Khivantsev et al. have reported the electronic energies for binding NO to Pd^{2+} and Pd^+ cations as − 226 kJ/mol and − 192 kJ/mol, respectively [24]. However, Paolucci et al. have found that NO binding energies are highly sensitive to the choice of density functional and that using GGA functionals can overestimate the NO binding strength by up to 99 kJ/mol; hence, these authors report calculated NO binding energies of − 175 kJ/mol for Pd^+ and − 70 kJ/mol for Pd^{2+} using the hybrid HSE06 functional [25].

Adsorption of NO on $[Pd(OH)]^+$ sites in Pd-exchanged zeolites has also been proposed [1,26,27]. It has been suggested that $[Pd(OH)]^+$ is involved in the adsorption of NO, either as an adsorption site or as a precursor to the formation of Pd^+ according to the reaction: $NO + 2Z^-[Pd(OH)]^+ \leftrightarrow 2Z^-Pd^+ + NO_2 + H_2O$ [26,28]. On the other hand, Mandal et al. have concluded that $[Pd(OH)]^+$ does not form on samples with Pd content lower than the number of paired Al sites, as supported by DFT calculations and the absence of $[Pd(OH)]^+$ bands in IR spectra of Pd/H-CHA acquired before and after NO [25]. We also note that Khivantsev et al. have suggested that $[Pd(OH)]^+$ adsorbs NO to form $[Pd(OH)(NO)]^+$ [15]. However, DFT studies reported by Van der Mynsbrugge et al. suggest that in the presence of air and water, Pd^+/H^+ and Pd^{2+} associated with pairs of Al atoms in the 6-rings and 8-rings of CHA are the thermodynamically favored species [29]. These calculations also show that the stability of $[Pd(OH)]^+$ is lower than that of Pd^{2+} and Pd^+/H^+ at Al pair sites, and under the conditions used in experimental studies $[Pd(OH)]^+$ would readily react with the adjacent H^+ to form a Pd^{2+} and water.

The influence of other gas phase species on the adsorption of NO has also been studied. Water vapor present during NO adsorption has been reported to facilitate the mobility of PdO particles, leading to redispersion of Pd as cations [13], and water vapor has also been found to displace adsorbed NO from both the zeolite and Pd cations [30]. Oxygen, another component present in automotive exhaust, can also impact NO adsorption by forming NO_2, which has been reported as a product upon NO desorption as well as an increase in the IR band associated with NO^+ on Pd/H-ZSM-5 [11]. Oxygen also prevents the reduction of Pd cations to small Pd particles, which do not adsorb NO [11,15]. Additionally, heating Pd-exchanged zeolites in O_2 has been shown to convert metallic Pd nanoparticles to isolated Pd cations, thereby restoring the NO adsorption capacity of a PNA following use [31].

Another factor influencing the adsorption of NO is the location where Pd cations are exchanged into CHA. A recent theoretical study has shown that the relative stability Pd^{2+} and Pd^+ in cation-exchange sites in CHA strongly depends on the location of the Al atoms in the framework, as well as the operating conditions (e.g., exposure to water) [29] Next-next-nearest neighbor (NNNN) Al pairs (separated by two Si atoms) in the 6-membered ring provide four zeolite oxygen atoms to coordinate Pd^{2+} cations in an ideal square planar configuration. As a result, Pd^{2+} is significantly more stable than Pd^+ at these Al pairs, over a wide range of conditions. By contrast, next-nearest neighbor (NNN) Al pairs (separated by a single Si atom) cannot provide the ideal square planar coordination to stabilize Pd^{2+}, such that the relative stability of Pd^+ and Pd^{2+} cations at these Al pairs depends on the temperature and partial pressure of water. The relative amounts of Pd^+ and Pd^{2+} cations exchanged at NNN Al pairs can therefore be altered by varying the temperature and partial pressure of water. The question of whether or not Pd^+ is present in as-prepared and pretreated Pd/CHA remains open, as several authors have suggested based on evidence inferred from IR spectroscopy that Pd^+ only forms upon NO adsorption via the process $Pd^{2+}(Z^-)_2 + 2\ NO \rightarrow (NO)\ Pd^+\ Z^- + NO^+Z^-$; however, direct evidence of Pd^+ in zeolites in the absence of adsorbates has been reported by electron paramagnetic resonance spectroscopy (EPR) [15,28,32].

The zeolite support onto which Pd cations are exchanged can also adsorb NO; hence, it is important to understand what fraction of the NO adsorbed in a PNA material is associated with the zeolite. IR spectroscopy has been used to identify the NO adsorption site in zeolites [33]. The principal feature observed in H-SSZ-13 (H-CHA) is a band at 2160 cm^{-1} ascribed to NO^+Z^-. It has been suggested that this species forms via the reaction of two NO molecules (or NO and NO_2) with two Brønsted acid sites via $2\ NO + 2\ H^+Z^- \rightarrow 2\ NO^+Z^- + H_2$ or via $NO + NO_2 + 2\ H^+Z^- \rightarrow 2\ NO^+Z^- + H_2O$. The importance of proximate pairs of anion exchange sites to adsorb NO on acid sites in the zeolite has also been reported [34].

The present study was undertaken with the aim of identifying NO adsorption sites on Pd/H-CHA and investigating the effect of water vapor and oxygen on the sites to which NO adsorbs. This effort has combined experimental studies and theoretical analysis based on DFT calculations. The questions addressed are the effects of adsorbent pretreatment on the formation of NO adsorption sites on both H-CHA and Pd/H-CHA, the relation between the oxidation state of Pd cations and the strength of NO adsorption, the vibrational frequencies for adsorbed NO on various binding sites, and the influence of H_2O and O_2 on NO adsorption on both H-CHA and Pd/H-CHA. The effects of gas composition and temperature on the reduction of Pd^{2+} to Pd^+ and the reverse oxidation reaction are also examined.

2. Methods

2.1. Adsorbent synthesis and characterization

The CHA zeolite (Si/Al = 12) was provided by BASF. This zeolite was the support utilized for the experiments described below. Additional CHA zeolite (Si/Al = 14) was prepared and used in experiments presented in the supplemental material. Palladium-exchanged zeolites were prepared by incipient wetness impregnation.[23] De-ionized water (18.2 MΩ) was added drop-wise to the NH_4-form zeolite while stirring until the total pore volume reached saturation, evidenced by a transformation from a powder-like substance to a liquid-like slurry. Assuming the same mass uptake as water, a $Pd(NH_3)_4(NO_3)_2$ solution (10 wt%, Sigma-Aldrich) was appropriately diluted with de-ionized water (18.2 MΩ) to achieve a desired Pd loading, using the same deposition procedure for the water-only trial. The Pd-form zeolite was dried in an oven at 393 K before treating in flowing air (Air Zero, Indiana Oxygen, 6000 $cm^3\ h^{-1}\ g^{-1}$) to 823 K (120 K h^{-1}) for 5 h.

The framework topology was characterized with *ex situ* powder XRD, using a Rigaku Smartlab X-ray Diffractometer. Samples (0.01 g) were pressed onto low-dead volume holder (Rigaku), and patterns were collected from 4° to 40° 2θ with a scan rate of 60° h^{-1} and a resolution of 0.01°.

Atomic absorption spectroscopy (AAS) was used to quantify the elemental contents using a Perkin Elmer model Analyst 300. Samples (0.02–0.05 g) were digested with 2.5 g of hydrofluoric acid (48 wt%, Alfa Aesar) for 3 days before diluting with 50 g of de-ionized water (18.2 MΩ). The Pd and Al contents in solution were determined by comparing to known elemental analysis standards. The Si/Al ratio was estimated by subtracting the contribution of extraframework cations and assuming a perfectly crystalline adsorbent with molar composition of $Si_{(1-x)}O_2Al_x$.

The amounts of cationic Pd and agglomerated PdO domains were quantified using H_2 temperature programmed reduction (TPR), using protocols we have reported previously [35]. H_2 TPR characterizations were performed with a Micromeritics Autochem II 2920 Chemisorption

Analyzer, and H_2 consumption was quantified with a thermal conductivity detector (TCD). A TCD response factor determined by flowing different partial pressures (0.1–5 kPa) of H_2 in balance Ar, of which quantified a Micromeritics Ag_2O standard within 10%. Zeolites (0.05–0.10 g) were pretreated in flowing air (Air Zero, Indiana Oxygen, 1800 $cm^3\ h^{-1}$) to 473 K, 823 K, or 1023 K (600 K h^{-1}) for 1 h, cooled to 373 K before replacing the Air stream with Ar (UHP, Indiana Oxygen), then cooled to 203 K using a Micromeritics Cyrocooler II accessory. The Ar stream was replaced with 5 kPa H_2 in balance Ar (600 $cm^3\ h^{-1}$), then after achieving a stable TCD signal, the sample was treated to 573 K (600 K h^{-1}). H_2 TPR profiles, quantifications, and discussion can be found in the Supplemental Material (Section S2).

2.2. Temperature-programmed desorption (TPD) studies

All TPD studies were conducted in a quartz reactor. Typically, 100 mg of adsorbent was loaded into the reactor. A quartz wool plug was placed below the bed to prevent the adsorbent from entering the effluent gas line. Before NO adsorption measurements, the adsorbent underwent hydrothermal aging (HTA) in a stream of air containing 5% water from 348 K to 773 K at 2 K/min. The temperature was held at 773 K for 5 h, and then cooled back to 348 K in the absence of water vapor.

For adsorption, a feed stream containing the adsorbate was flowed over the adsorbent at 348 K until adsorbent was saturated. The composition of the feed stream was adapted to the experiment. The feed typically consisted of about 200 ppm of NO in a He flowing at 250 mL/min. 1000 ppm CH_4 was added to the NO/He stream as an inert tracer. He (purity of 99.999% from Praxair) was dried by passage through moisture trap (Restek Moisture Trap, <10 ppb water) and NO (1.03% NO in He balance from Praxair) was purified by passage through traps to remove moisture and NO_2 (Alltech Gas Drier, <1 ppm NO_2 and H_2O). The air carrier gas provided by Praxair is rated as extra dry (<10 ppm H_2O). The adsorption of NO was monitored using an MKS 2030 Multigas analyzer, a non-dispersive infrared (NDIR) spectroscopy instrument. The concentration of NO in the effluent was measured, and the NO and CH_4 were shut off once the effluent concentration of NO had reached the inlet value. The adsorbent was then purged with He until the concentration of NO had returned to the level observed before the start of the adsorption step. A purge stream of He (250 mL/min) was fed to the reactor immediately after adsorption to remove any weakly bound adsorbates. The adsorbed NO was desorbed while the adsorbent was heated from 348 K to 773 K at 10 K/min, and then held at 773 K for 20 min. Throughout this period the concentration of NO and NO_2 in the effluent was monitored by the Multigas analyzer. Following a TPD experiment, the adsorbent was treated in one of several ways in order to prepare it for the next adsorption cycle. This typically involved cooling the adsorbent from 773 K back to 348 K in a defined gas mixture (e.g., He, air, air plus water vapor). This last step is referred to as a pretreatment, and for future discussion, the pretreatment refers to the step performed before an adsorption measurement when the adsorbent undergoes several adsorption/desorption cycles. In this study, cycles typically refer to repeated experiments on the same adsorbent loading.

2.3. IR spectroscopy

The procedure for the initial treatment of Pd/H-CHA and pretreatment between NO adsorption experiments is similar to that used for the TPD experiments. About 30 mg of adsorbent was compressed into a pellet that was placed into a Harrick High Temperature cell with CaF_2 windows. The cell was heated resistively and the temperature was monitored with a thermocouple. The adsorbent was exposed to NO for 15 min, after which the NO flow was stopped and the TPD ramp was started. *In situ* transmission IR experiments were conducted using a Nicolet 6700 spectrometer operated at 4 cm^{-1} resolution. Each spectrum is obtained by averaging 256 scans. Background spectra of Pd/H-CHA, taken at the same temperatures as those at which spectra were recorded during a TPD IR experiment, were subtracted from the spectra of NO adsorbed on Pd-CHA. Additional baseline subtraction was conducted using Origin.

2.4. Theoretical calculations

The crystallographic structure of CHA was obtained from the database maintained by the International Zeolite Association (IZA) [36]. A large cluster model containing 696 tetrahedral atoms (T696) was constructed by selecting the framework atoms within a 25 Å radius of a central *cha* cage, and trimming the edges of the resulting fragment such that the cluster is terminated by double six-ring units. This large model avoids any boundary effects and prevents the introduction of unintended anisotropy in the description of long-range interactions [37].

Al pairs were placed in various next-nearest neighbor (NNN), next-next-nearest neighbor (NNNN) or next-next-next-nearest neighbor (NNNNN) configurations in the CHA framework. The resulting double charge defects were compensated by either Pd^+/H^+ or Pd^{2+}. A total of 16 structures in which the Pd cations are accessible from the *cha* cage were selected to model potential NO adsorption sites. A hybrid quantum mechanics/molecular mechanics (QM/MM) approach was applied to limit the computational expense. A smaller fragment of the zeolite cluster and the adsorbates are treated quantum mechanically (QM), using the range-separated hybrid functional ωB97X-D [38,39], combined with def2 basis sets, which include an effective core potential for Pd. The QM region includes all neighboring T-atoms of each Al, as well as all Si and O atoms that are part of the 4-, 6-or 8-ring(s) connecting the pair of Al atoms. Where necessary, the QM region was extended further to fully account for the interactions of adsorbed NO with the zeolite framework. The remainder of the large cluster model is treated using molecular mechanics (MM) [40,41]. Fig. 1 shows the T696 cluster model and highlights the 4-, 6- and 8-rings facing the *cha* cages. Geometry optimizations and frequency calculations are performed at the ωB97X-D/def2-SV(P) level of theory, followed by single-point energy refinements at the ωB97M-V/def2-TZVPD level of theory. Paolucci et al. have pointed out that binding energies of NO to Pd are particularly sensitive to the choice of density functional [25]. In this study, we have selected the range-separated hybrid meta GGA functional ωB97M-V[43] to evaluate the energetics, because it has emerged as the overall best performer out of the 200 density functionals evaluated by Mardirossian and Head-Gordon [42]. The MM region is described with a CHARMM-type force field using the P2 parameter set [41]. Initial geometries were constructed with ZEOBUILDER [43]. All QM/MM calculations were performed with a developmental version of Q-Chem [44]. Thermochemical quantities are calculated from a normal mode analysis using the quasi-rigid rotor/harmonic oscillator approximation (RRHO) [41,45] on the optimized structures.

3. Results

3.1. NO adsorption on H-CHA

NO adsorption on H-CHA (SiAl = 12) was examined in order to characterize its interaction with the zeolite support. Fig. 2 shows the TPD profile after NO adsorption on H-CHA. Both NO and NO_2 were observed in the effluent in the ratio of 2/1, and the total amount of NO adsorbed is 5.4 μmol NO per gram of adsorbent. This amount of adsorbed NO corresponds to about 7.3×10^{-3} mol NO_x per mole of protons, indicating that only a small fraction of the zeolitic protons are involved in NO adsorption.

Fig. 2 also shows the IR spectra taken during TPD. At 348 K, the peaks observed are the result of NO adsorption on H-CHA. The peak at 2160 cm^{-1}, due to NO^+Z^-, appears to be comprised of two components, reflecting somewhat different environments [34,46]. The appearance of this band is accompanied by a decrease in the peak at 3590 cm^{-1} peak due to Brønsted acidic O-H stretches [34]. There is also an increase in a

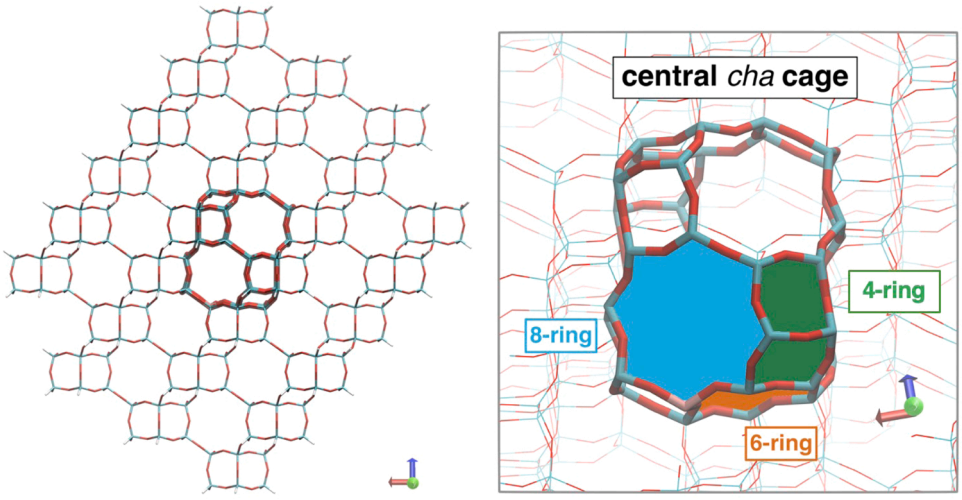

Fig. 1. Left: T696 cluster model for CHA used in QM/MM calculations. Si atoms are represented in cyan, Al in pink, O in red, H in white. The central CHA cage containing the adsorption sites is shown in bold lines. Right: 6-, 8- and 4-rings in *cha* cage.

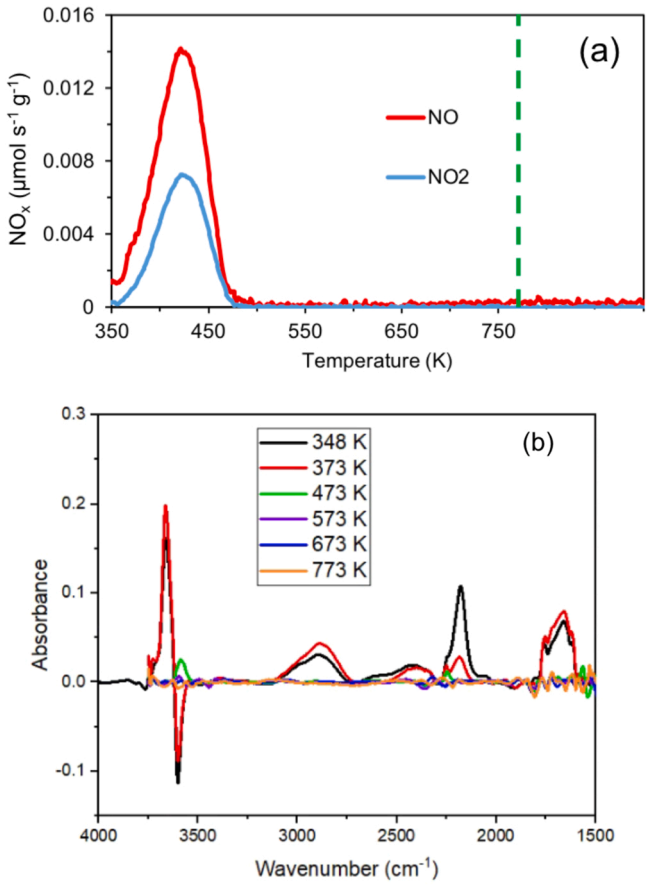

Fig. 2. NO/NO_2 TPD profiles (a) and TPD IR spectra (b) for NO adsorbed on H-CHA. H-CHA was heated in air from 348 K to 773 K at 2 K/min and held at 773 K for 1 h. The sample was then cooled in air from 773 K to 348 K. Adsorption was from a flow of He (250 mL/min) containing 200 ppm of NO at 348 K. During TPD, the temperature was ramped from 348 K to 773 K at 10 K/min and then held at 773 K for 20 min in He. The dashed line corresponds to the maximum temperature of 773 K; the TPD profile beyond this line represents the continued temporal evolution of the system at constant temperature. Nearly identical results were obtained over four adsorption-desorption cycles. For the IR spectra, a reference spectrum was taken of H-CHA before NO adsorption, and then subtracted from the spectrum taken after NO adsorption. Scans were taken every 100 K during which the temperature was ramped at 2.5 K/min in He.

peak 3670 cm^{-1}, which is assigned to water adsorbed on the zeolite [47]. Additional evidence for the formation of water upon NO adsorption is the appearance of broad bands located 2830 cm^{-1}, 2390 cm^{-1}, and 1630 cm^{-1}, all of which have been reported for water strongly hydrogen bonded to Brønsted acid sites in H-CHA [47–49]. We note that the shape of the broad centered at 1630 cm^{-1} does not match that expected for water vapor adsorbed on H-CHA, suggesting the presence of other species such as nitrates. The broad feature between 1500 and 1700 cm^{-1} may also contain contributions from nitroso (NO_2^-) and nitrates (NO_3^-) [26,47,50,51]. These latter species very likely form during adsorption via the reaction of NO with small amounts of O_2 retained on the sample from the pretreatment in air. During TPD, the features associated with adsorbed NO and H_2O are retained when the temperature rises to 373 K, but by 473 K, all of the peaks have disappeared. This pattern is consistent with the TPD profile presented in Fig. 2a, which shows that all NO and NO_2 desorbs by 473 K. It is also notable that the band at 3590 cm^{-1} for Brønsted acidic OH groups is restored during desorption of NO, suggesting that these species are associated with in the adsorption of NO. This conclusion is confirmed by the observation that the TPD profile in the TPD IR spectra in Fig. 2b is reproducible after multiple adsorption and desorption cycles. Hadjiivanov et al. has proposed that NO and NO_2 react with two nearby Brønsted acid sites to form two NO^+ bound to the zeolite, as well as a water molecule that is H-bonded to another Brønsted acid site [34].

The effect of water on NO adsorption on H-CHA was also investigated. To explore these effects, NO was first adsorbed on H-CHA by exposure to 200 ppm of NO in He, and then to a He stream containing 1% water for 10–20 min. After that, the sweep gas was switched to He and the temperature was ramped from 348 K to 773 K. Exposure of the pre-adsorbed NO to water resulted in the disappearance of the peaks for NO and NO_2 in the TPD profile. This figure is reported in the SI (Fig. S2). These results are similar to those reported for zeolite BEA, which have shown that water displaces NO adsorbed on the zeolite [30]. In addition, the inclusion of water in the pretreatment also prevented any NO adsorption on H-CHA. As a result, the experiments presented in Figs. 2 and 3 are done for NO adsorption pretreated in air.

The effect of air on the adsorption of NO on H-CHA was also examined. As seen in Fig. 3a, the adsorption of NO from air resulted in the desorption of nearly equivalent amounts of NO and NO_2 during TPD. The total amount of NO_x adsorbed (as either NO or NO_2) in this case is 63 μmol of NO_x per gram of adsorbent (5.7×10^{-2} mol NO/mol protons), which is considerably higher than the amount for NO adsorbed from He, 5.4 μmol NO_x/g of adsorbent (7.3×10^{-3} mol NO_x/mol protons) [34]. The appearance of equivalent amounts of NO and NO_2 during

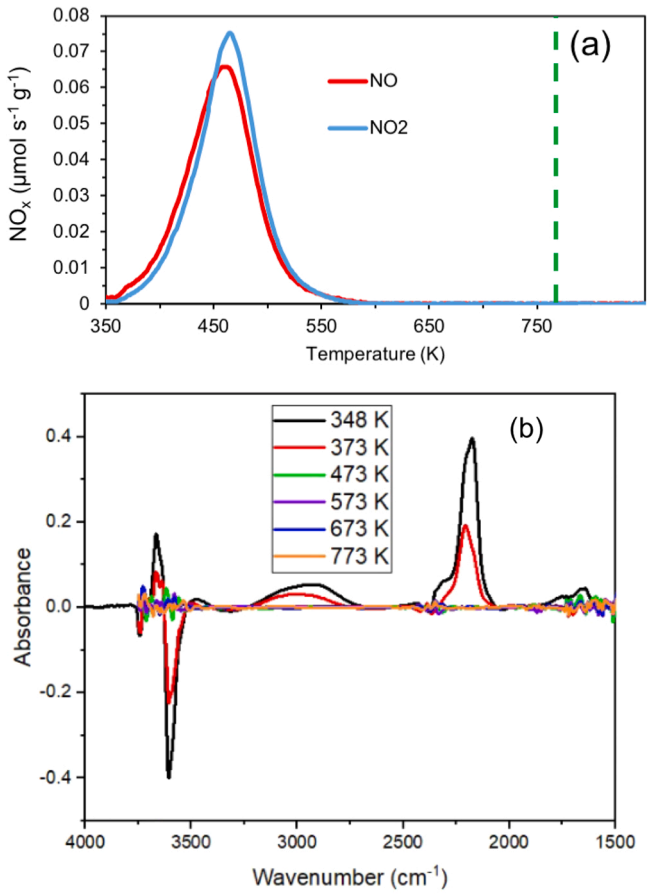

Fig. 3. NO/NO_2 TPD profiles (a) and TPD IR spectra (b) for NO adsorbed on H-CHA. H-CHA was heated in air 348 K to 773 K at 2 K/min and held at 773 K for 1 h. The sample was then cooled in air from 773 K to 348 K. Adsorption was from a flow of air (250 mL/min) containing 200 ppm of NO at 348 K. During TPD, the temperature was ramped from 348 K to 773 K at 10 K/min and then held at 773 K for 20 min in air. The dashed line corresponds to the maximum temperature of 773 K; the TPD profile beyond this line represents the continued temporal evolution of the system at constant temperature. Nearly identical results were obtained over four adsorption-desorption cycles. For the IR spectra, a reference spectrum was taken of H-CHA before NO adsorption, and then subtracted from the spectrum taken after NO adsorption. Scans were taken every 100 K during which the temperature was ramped at 2.5 K/min.

TPD suggests that a fraction of the desorbing NO undergoes oxidation to NO_2.

The TPD IR spectra for NO adsorbed from air onto H-CHA are shown in Fig. 3b. Similar to the TPD IR results for the case of NO adsorbed from He (Fig. 2b), all of the bands disappear by 473 K. There is a sharp band at 2160 cm^{-1} due to NO^+ adsorbed on the zeolite, and a corresponding negative band at 3590 cm^{-1} indicating the loss of Brønsted acid sites. The band at 2160 cm^{-1} is also more intense when NO is adsorbed from air, supporting the mechanism proposed by Hadjiivanov et al. [34]. When NO is adsorbed from air, the integrated area of the band for NO^+ is 4.8 times higher than that for NO adsorption from He, while the integrated area of the band for water around 2890 cm^{-1} is about 3.0 times higher, which agrees semi-quantitatively with what would be expected [34].

3.2. NO Adsorption on Pd/H-CHA

The adsorption of NO on Pd/H-CHA (SiAl = 12, PdAl = 0.24) was investigated in order to identify the different states of NO adsorbed on Pd cations and the influence of adsorbent pretreatment on the distribution of these states of adsorbed NO. For these experiments, the adsorbent was first heated to 773 K at 2 K/min in air containing 5% H_2O, held at this temperature for 5 h, and then cooled to 348 K in air (not containing water vapor). This pretreatment was chosen to attempt to maximize the amount of isolated Pd [1]. As seen in Fig. 4a, the TPD profile for NO adsorbed on Pd/H-CHA exhibits two prominent NO desorption peaks: a low-temperature peak around 423–473 K and a broad high-temperature peak ranging from 550 to 900 K with a maximum at about 753 K. The low-temperature peak comprises 29% of the desorbing NO and the high-temperature peak comprises 71%. No NO_2 was observed in the effluent during TPD. The total amount of NO adsorbed on Pd/H-CHA is about 57 μmol of NO per gram of adsorbent, which corresponds to a NO/Pd ratio of 0.73. This ratio agrees well with the fraction of isolated cations present in Pd/H-CHA measured by H_2 temperature programmed reduction (0.79), suggesting that each Pd cation adsorbs one NO molecule.

Fig. 4b shows the IR TPD spectra for NO adsorbed on Pd/H-CHA. For this experiment, the adsorbent was heated to 773 K at 2 K/min in a flow of air containing 5% H_2O and then held at this temperature for 5 h, and then cooled to 348 K in air (not containing water vapor) and held at this

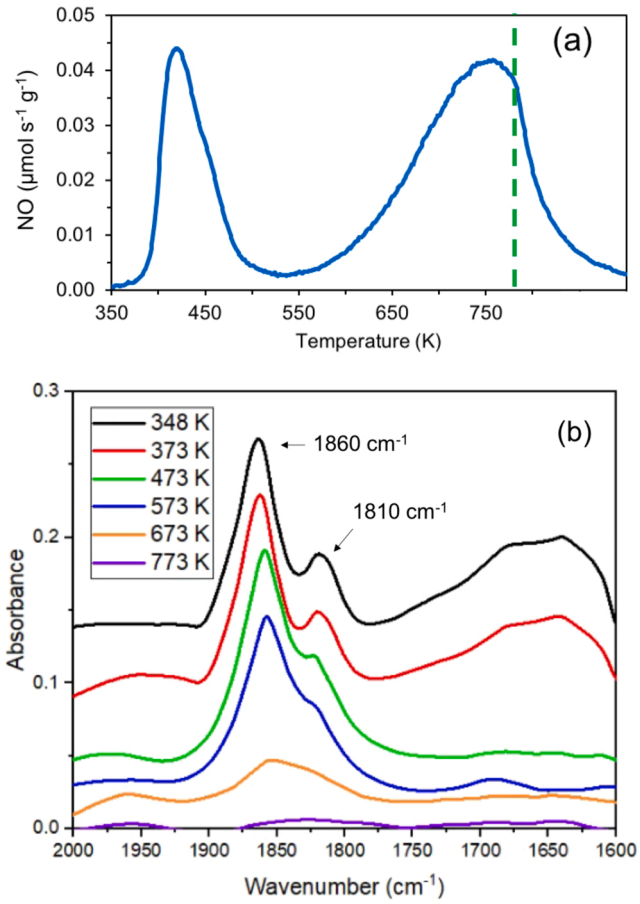

Fig. 4. The NO TPD profile (a) and the TPD IR spectra (b) for NO adsorbed on Pd/H-CHA. Pd/H-CHA was heated in air and 5% H_2O from 348 K to 773 K at 2 K/min and held at 773 K for 5 h. The sample was the cooled in He and 5% H_2O from 773 K to 348 K. NO adsorption was from a flow of He (250 mL/min) containing 200 ppm of NO at 348 K. During TPD, the temperature was ramped from 348 K to 773 K at 10 K/min and then held at 773 K for 20 min in He. The dashed line corresponds to the maximum temperature of 773 K; the TPD profile beyond this line represents the continued temporal evolution of the system at constant temperature. Nearly identical results were obtained over four adsorption-desorption cycles. For the IR spectra, a reference spectrum was taken of Pd/H-CHA before NO adsorption, and then subtracted from the spectrum taken after NO adsorption. Scans were taken every 100 K during which the temperature was ramped at 2.5 K/min.

temperature for 5 h. After pretreatment, the sample was exposed to about 200 ppm NO in He for about 15 min. The principal peaks associated with adsorbed NO occur at 1860 cm^{-1} and 1810 cm^{-1}. Notably, the peak at 2160 cm^{-1} for NO^+Z^- is absent. We attribute this to the retention of water vapor from the pretreatment step, which inhibits NO adsorption on the zeolite to form NO^+Z^- [30]. The peaks at 1860 cm^{-1} and 1810 cm^{-1} have been observed previously in the IR spectrum of NO adsorbed on Pd-SSZ-13 and have been assigned to NO adsorbed on Pd^{2+} and Pd^+ cations, respectively, on the basis of DFT calculations [28]. The absence of a band at 2160 cm^{-1} for zeolite-bound NO^+, a consequence of the pretreatment of Pd/H-CHA in a He/H_2O mixture, indicates that all of the NO_x that desorbs during the TPD of Pd/H-CHA comes from NO adsorbed on Pd cations. As shown earlier, pre-exposure of H-CHA to H_2O inhibits via site-blocking the adsorption of NO as NO^+Z^-. Fig. 4b also shows a broad band around 1600–1775 cm^{-1} attributable to water adsorbed on the zeolite during the pretreatment step. This band is also observed prior to NO adsorption, and very little NO_2 is observed during TPD. It's likely that most of this band is adsorbed water and adsorbed nitrates do not contribute significantly [26].

IR TPD experiments were performed to observe how the band intensities change as a function of temperature. Fig. 4b shows that the broad band at 1650 cm^{-1}, due to water adsorbed on the zeolite disappears between 358 K and 473 K, in agreement with previous observations [34,47]. More notably, the band at 1810 cm^{-1} undergoes a significant loss in intensity above 373 K and loses most of its intensity by about 573 K. By contrast, the band at 1860 cm^{-1} band only begins to lose intensity above 573 K and is no longer visible by 773 K. The relationship between band assignment and TPD behavior will be discussed in Section 3.5.

3.3. Effect of water on NO adsorption

Water vapor has been reported to affect the TPD profile of NO adsorbed on Pd-BEA. Khivantsev et al. have shown that when NO is co-adsorbed with O_2 and H_2O, only a high-temperature NO TPD feature is observed > 473 K, and Chen et al. have shown that water displaces the NO species responsible for the IR band at 1860 cm^{-1} [15,30]. Consequently, we undertook experiments to assess whether water displaces either of the two forms of adsorbed NO observed during TPD and IR spectroscopy. The results of these experiments combined with theoretical analysis, enabled identification of the Pd species on which NO is adsorbed and the effects of water on the stability of adsorbed NO. Pd/H-CHA was pretreated by feeding a stream of air containing 5% water from 348 K to 773 K at 2 K/min. The temperature was held at 773 K for 5 h, and then cooled back to 348 K in the absence of water vapor After pretreatment, Pd/H-CHA was exposed to 200 ppm of NO in He, and then to a He stream containing 1% water for 20 min. After that, the sweep gas was switched to He and the temperature was ramped from 348 K to 773 K. Fig. 5a shows that exposure of the sample containing adsorbed NO to water vapor caused a complete disappearance of the low-temperature NO desorption peak, but had no effect on the desorption of NO at higher temperatures. Fig. 5b also shows that pre-adsorbed NO desorbed from the sample almost immediately after it was exposed to the He stream containing water vapor. In fact, the amount of NO displaced by water vapor (12 μmol NO per g of adsorbent and 0.15 NO/Pd) corresponds closely to the amount of NO that would have desorbed in the low temperature NO desorption peak in the absence of water exposure (16 μmol NO per g of adsorbent and 0.21 NO/Pd).

Fig. 6a shows IR spectra of NO adsorbed on Pd/H-CHA taken before and after exposure of the sample to water vapor. The spectrum recorded prior to water vapor exposure is identical to that shown in Fig. 4b. After exposure to water vapor, the band at 1630 cm^{-1} sharpens due to water adsorption onto the Brønsted acid sites [34]. The band centered at 1860 cm^{-1} loses intensity; however, the band at 1810 cm^{-1} is unaffected. Similar results have been reported by Mandal et al., who found that increasing the concentration of water in the feed preferentially reduces the intensity of the 1860 cm^{-1} band compared to the 1810 cm^{-1} band [25]. The loss in intensity of the band at 1860 cm^{-1} during water adsorption and the lack of NO desorption at low temperatures suggests that a portion of the adsorbed NO contributing to the band at 1860 cm^{-1} also contributes to low-temperature NO desorption. The band at 1860 cm^{-1} does not disappear completely, suggesting that it may comprise multiples forms of adsorbed NO associated with Pd cations, as will be discussed below. The absence of an effect of water exposure on the band at 1810 cm^{-1} suggests that the NO-Pd species contributing to this band and the part of the 1860 cm^{-1} band unaffected by water vapor are responsible for the NO desorption observed above 500 K.

Fig. 6b also shows the IR spectra of adsorbed NO taken during TPD following the exposure of adsorbed NO to water vapor. The band for water adsorbed on the zeolite disappears completely, as soon as the temperature increases above 373 K. The bands remaining at 1860 cm^{-1} and 1810 cm^{-1} follow a pattern very similar to that shown in Fig. 4b. With increasing temperature, the band at 1810 cm^{-1} decreases first and loses intensity before the band at 1860 cm^{-1} loses intensity. All band intensity is lost by 773 K.

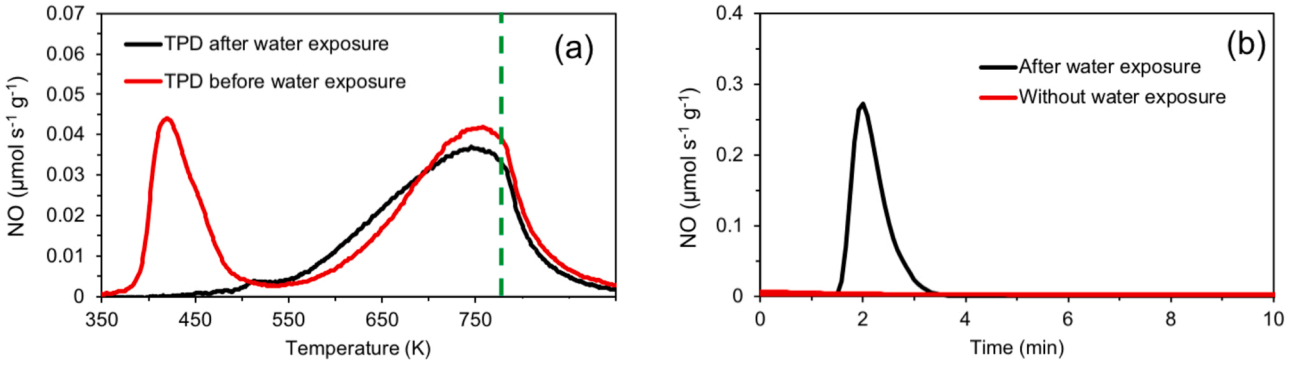

Fig. 5. (a) NO TPD profile for Pd/H-CHA without and with exposure of adsorbed NO to water vapor prior to the onset of TPD. (b) The desorption of NO caused by exposure of NO adsorbed on Pd/H-CHA prior to the onset of TPD. Pd/H-CHA was heated in air and 5% H_2O from 348 K to 773 K at 2 K/min and held at 773 K for 5 h. After heating, the sample was cooled in He and 5% H_2O from 773 K to 348 K. NO adsorption was from a flow of He (250 mL/min) containing 200 ppm of NO at 348 K. To observe the effects of water vapor on adsorbed NO on Pd/H-CHA, the flow of NO in He was stopped and replaced by a He flow constraining 5% H_2O at 348 K. The water exposure was held for 20 min, after which the water flow was stopped and TPD started. During TPD, the temperature was ramped from 348 K to 773 K at 10 K/min and then held at 773 K for 20 min in He. The dashed line corresponds to the maximum temperature of 773 K; the TPD profile beyond this line represents the continued temporal evolution of the system at constant temperature.

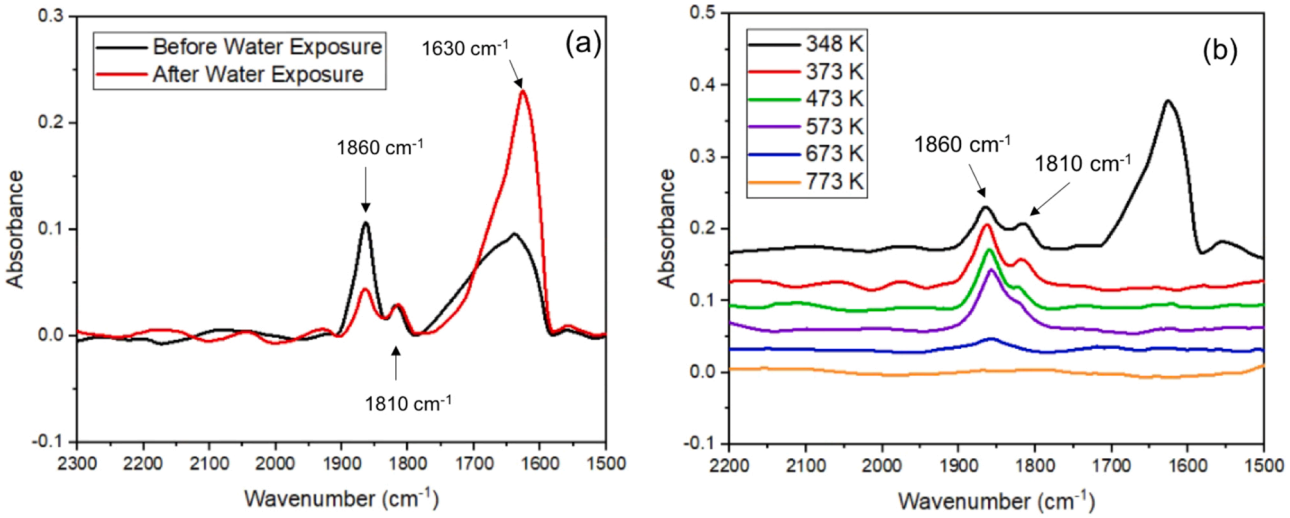

Fig. 6. IR spectra (a) and TPD IR profiles (b) for NO adsorbed on Pd/H-CHA. Pd/H-CHA was heated in air and 5% H_2O 348 K to 773 K at 2 K/min and then held at 773 K for 5 h. After heating, the sample was cooled in He and 5% H_2O from 773 K to 348 K. NO adsorption was from a flow of He (250 mL/min) containing 200 ppm of NO at 348 K. To observe the effects of water vapor on adsorbed NO on Pd/H-CHA, the flow of NO in He was stopped and replaced by a He flow constraining 5% H_2O at 348 K. The water exposure was held for 20 min, after which the water flow was stopped and the acquisition of TPD IR spectra was initiated. During TPD IR, the temperature was ramped from 348 K to 773 K at 10 K/min and then held at 773 K for 20 min in He.

3.4. Effect of air on the adsorption of NO on Pd/H-CHA

Since air is present in automobile exhaust gas, it is important to determine how air affects the adsorption of NO on Pd/H-CHA. For these experiments, NO was adsorbed on Pd/H-CHA from flowing air stream using the same protocol described above for the adsorption of NO on H-CHA. The results of these experiments are shown in Fig. 7.

When NO is adsorbed from air, the TPD profile shows prominent peaks for NO and NO_2 centered at about 450 K. A smaller, broad feature is also observed for both species centered at about 575 K, but a large peak centered at 750 K is not observed, as otherwise appears in the TPD profile of NO adsorbed from He (Fig. 4b). The total amount of NO desorbing as either NO or NO_2 is 99 μmol/g of adsorbent, which is 1.7 times larger than that for NO adsorbed on Pd/H-CHA from He. Also plotted for comparison is the TPD profile for NO adsorbed from air taken for H-CHA (see Fig. 3). While the shape and position of the low-temperature features for NO and NO_2 are similar for Pd/H-CHA and H-CHA, the amounts desorbed are smaller. As noted earlier, the amounts of NO and NO_2 desorbed from H-CHA are 31 μmol per gram of adsorbent and 32 μmol per gram of adsorbent, respectively. This comparison suggests that roughly one third of the NO/NO_2 desorbing from Pd/H-CHA may be due to NO/NO_2 adsorption on the zeolite.

An IR spectrum of NO adsorbed on Pd/H-CHA from air is shown in Fig. 8a, and the same IR bands are present as were observed in the spectrum for NO adsorbed from He (Fig. 4b), except that the band at 2160 cm^{-1} is now significantly more intense. There is a small broad band around 1630 cm^{-1}, attributable to water produced during the formation of NO^+Z^- and to nitrates formed via the reaction of NO with O_2 during NO adsorption [26,34,50,51]. We also note that the appearance of this band is accompanied by a loss in Brønsted acidic O-H intensity upon NO adsorption. These features are similar to those seen in Fig. 3 for the adsorption of NO from air on H-CHA. Fig. 8a also shows an apparent increase in the intensity of band at 1810 cm^{-1} relative to that observed for the case of NO adsorption from He. The increase is designated as apparent because a new, broad band appears beneath the feature at 1810 cm^{-1}, which on the low-wavenumber side extends to 1750 cm^{-1}. The identity of this band is not known. Fig. 8b shows the TPD IR spectra taken during NO desorption from Pd/H-CHA in flowing air. As seen in the TPD IR spectrum for H-CHA (Fig. 2), the 2160 cm^{-1} band disappears by about 473 K, as does the broad feature at 1650 cm^{-1} attributed to adsorbed water (which is likely associated with NO^+ formation) [34]. The two bands at 1860 cm^{-1} and 1810 cm^{-1} attenuate in

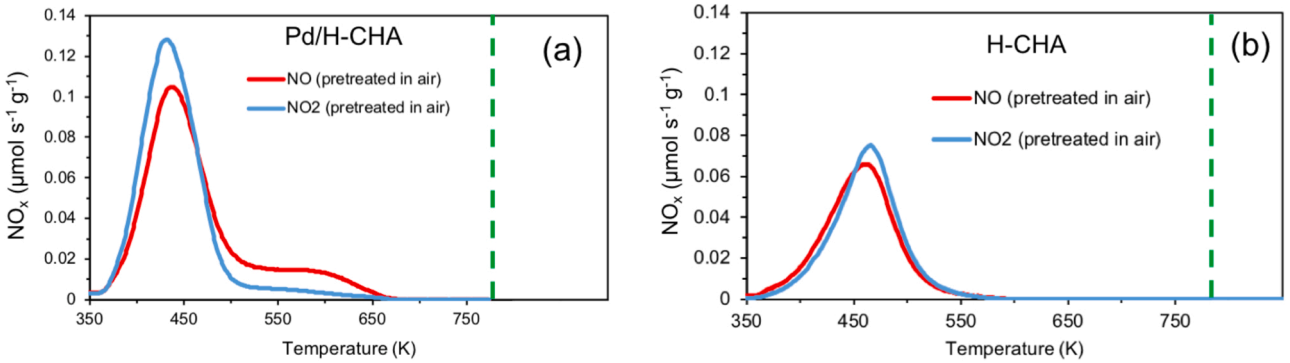

Fig. 7. Comparison of NO and NO_2 TPD profiles for NO adsorbed from air on Pd/H-CHA (a) and for NO adsorbed from air on H-CHA (b) Pd/H-CHA was heated in air and 5% H_2O from 348 K to 773 K at 2 K/min and then held at 773 K for 5 h. H-CHA was heated in air from 348 K to 773 K at 2 K/min and then held at 773 K for 1 h. Following initial heating, both samples were cooled in air from 773 K to 348 K. Adsorption was from a flow of air (250 mL/min) containing 200 ppm of NO at 348 K. During TPD, the temperature was ramped from 348 K to 773 K at 10 K/min and then held at 773 K for 20 min in air. The dashed line corresponds to the maximum temperature of 773 K; the TPD profile beyond this line represents the continued temporal evolution of the system at constant temperature.

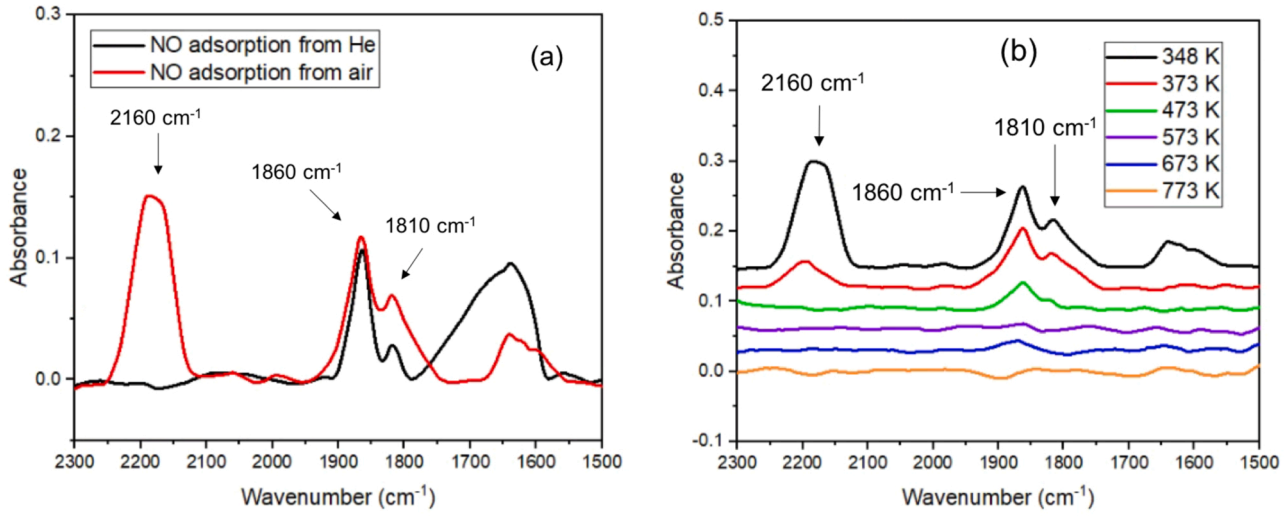

Fig. 8. (a) IR spectra of NO adsorbed from He or air on Pd/H-CHA. For the case of NO adsorption from He. Pd/H-CHA was heated in air and 5% H_2O from 348 to 773 K at 2 K/min and held at 773 K for 5 h. In 8a, for the NO adsorption from He, the sample was cooled in He and 5% H_2O from 773 K to 348 K. For the NO adsorption from air, the sample was cooled in air from 773 K to 348 K. Adsorption occurred at 348 K from a flow (250 mL/min) containing 200 ppm NO in He or air. A reference spectrum was taken of Pd/H-CHA before NO adsorption and then subtracted from the spectrum taken after NO adsorption. (b) TPD IR spectra taken during heating at a rate of 2.5 K/min in flowing air (250 mL/min).

a different manner compared to that seen in the IR TPD spectra shown in Fig. 4b for NO adsorbed onto Pd/H-CHA from He. Both the band centered at 1810 cm^{-1} and the one centered at 1860 cm^{-1} band disappear by around 573 K. This is consistent with the TPD results but differs from the experiment in which NO is adsorbed from He; there, the band at 1860 cm^{-1} does not disappear until higher temperatures. The observed effect of O_2 on the adsorption of NO on the zeolite as NO^+ cations is very similar to that reported by Hadjiivanov et al. for ZSM-5 [34]. The authors of this study propose that O_2 enhances the formation of NO^+ via the reaction $2\ H^+Z^- + 2\ NO + 0.5\ O_2 \rightarrow 2\ NO^+\ Z^- + H_2O$. An assessment of this possibility and alternatives are discussed below.

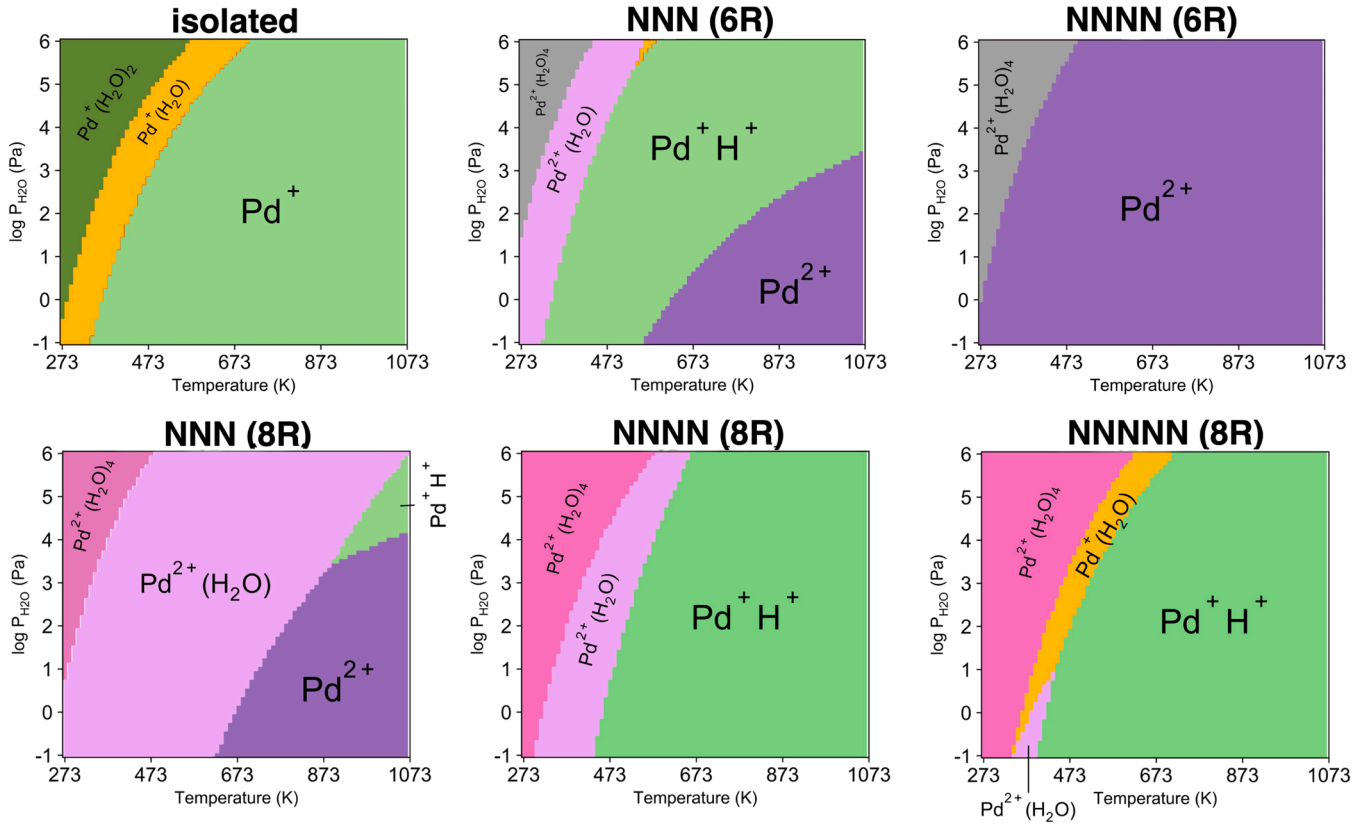

Fig. 9. [P_{H2O}, T] phase diagrams showing the thermodynamically preferred Pd species at isolated Al and next-nearest neighbor (NNN), next-next-nearest (NNNN) neighbor and next-next-next-nearest neighbor NNNNN) Al pair in the 6- and 8-rings of CHA under flowing air (P_{O2} = 20 kPa).
Reprinted with permission from ref.[29].

3.5. Theoretical Interpretation

3.5.1. NO adsorption in Pd/H-CHA

To elucidate which forms of adsorbed NO contribute to the low-temperature and high-temperature features observed in the TPD experiments (see Fig. 4b), as well as the different peaks observed in the transmission IR experiments, we have performed theoretical calculations of NO adsorption on a variety of Pd^{+} and Pd^{2+} sites that can be expected to be present in Pd/H-CHA after the pretreatment in wet air (T = 773 K and P_{H2O} = 5 kPa). In a recent theoretical study, we have shown that in the presence of air and water, Pd dispersed as Pd^{+} and Pd^{2+} cations is thermodynamically most favorable at Al pairs in the 6-rings and 8-rings in CHA [29]. The speciation of Pd was found to be more sensitive to the partial pressure of water than that of oxygen. Additionally, the preference for Pd^{+} or Pd^{2+} was found to depend strongly on the precise configuration of the Al pair. These findings are illustrated in the phase diagrams shown in Fig. 9. Because the NNNN Al pairs in the 6-ring allow for a near-perfect square planar coordination of the Pd^{2+} cation with four framework oxygen atoms, Pd^{2+} is lower in free energy than the next most favorable species at the NNNN Al pair by > 30 kJ/mol over a wide range of conditions. Consequently, it can be considered unchangeable throughout repeated adsorption-desorption-regeneration cycles on the Pd/H-CHA samples. By contrast, at NNN Al pairs in the 6-ring or 8-ring, Pd^{2+} and Pd^{+}/H^{+} might be interconverted depending on the temperature and the water partial pressure. Finally, at NNNN and NNNNN Al pairs in the 8-ring, Pd^{+}/H^{+} is more favorable than Pd^{2+}, as the Al atoms in these configurations are too far apart to efficiently stabilize a single divalent cation.

In this study, we have examined NO adsorption and desorption from the Pd^{+} and Pd^{2+} sites predicted by the phase diagrams in Fig. 9 to be present at Al pairs in the 6-rings and 8-rings. Additionally, we have considered Pd^{+} and Pd^{2+} sites that may be present due to NNN Al pairs in the 4-rings and NNNN Al pairs spanning two or more adjacent rings, identified in a high-throughput study on the stability of Pd cation sites in zeolites by Aljama et al. [52]. In these structures, the charge-compensating Pd cations are also located in a nearby 6- or 8-ring, such that they are accessible to adsorbates in the *cha* cage. Table 1 shows for each of the Pd sites considered in this study the formation energy (ΔE_{form}) relative to the Brønsted acid protons at the same Al pair:

$$Pd_{(g)} + H^{+}H^{+}(Z^{-})_2 + 0.25\ O_{2(g)} \rightarrow Pd^{+}\ H^{+}(Z^{-})_2 + 0.5\ H_2O_{(g)} \quad (1)$$

$$Pd_{(g)} + H^{+}H^{+}(Z^{-})_2 + 0.5\ O_{2(g)} \rightarrow Pd^{2+}(Z^{-})_2 + H_2O_{(g)} \quad (2)$$

For all Al pairs except NNNN Al pairs in the 6-ring, the formation energy of $Pd^{+}H^{+}(Z^{-})_2$ is more negative than that of $Pd^{2+}(Z^{-})_2$. For the NNN Al pairs in the 6-ring and the 8-ring, the formation energy of $Pd^{+}H^{+}(Z^{-})_2$ is lower than that of $Pd^{2+}Z^{-}Z^{-}$ by 50 kJ/mol and 30 kJ/mol, respectively. As shown by the phase diagrams in Fig. 9, both Pd^{+} and Pd^{2+} sites may be present at these Al pairs, depending on the temperature and the partial pressure of water. By contrast, for the NNNN and NNNNN Al pairs in the 8-ring, for which the phase diagrams predict the presence of only Pd^{+} sites, the formation energy of $Pd^{+}H^{+}(Z^{-})_2$ is 165–199 kJ/mol lower than that of $Pd^{2+}(Z^{-})_2$. Consequently, we can reasonably expect that both Pd^{+} and Pd^{2+} sites may occur at the NNN Al pairs in the 4-ring and the NNNN Al pairs in adjacent rings for which the formation energy of $Pd^{2+}(Z^{-})_2$ is at most 50 kJ/mol higher than that of $Pd^{+}H^{+}(Z^{-})_2$. A schematic representation of the various Al pairs is included in the Supplemental Material (Fig. S5).

Table 1
Formation energies (ΔE_{form}) in kJ/mol for Pd^{+} and Pd^{2+} sites relative to the Brønsted acid protons at the same Al pair reported in ref. [29] (†) and ref. [52] (‡).

	$Pd^{+}\ H^{+}\ (Z^{-})_2$	$Pd^{2+}\ (Z^{-})_2$
6-ring†		
NNN	-266	-215
NNNN	-245	-303
8-ring†		
NNN	-220	-181
NNNN	-238	-74
NNNNN	-237	-38
4-ring‡		
NNN-1	-250	-154
NNN-2	-256	-233
other‡		
NNNN-1	-280	-270
NNNN-2	-284	-243
NNNN-3	-286	-263
NNNN-4	-271	-130
NNNN-5	-284	-143

To elucidate which NO adsorption modes contribute to the low-temperature and high-temperature features observed in the TPD experiments (see above, Fig. 4b), we have combined NO adsorption free energies ($\Delta G_{ads,NO}$) predicted by QM/MM for each of the potential sites with an equilibrium desorption model to estimate the temperature at which the desorption of NO reaches a maximum (T_{max}). Details on the calculation of the maximum desorption temperatures as well as XYZ coordinates of the optimized geometries of all NO adsorption complexes are included in the Supplemental Material (Section S3 and S6). To aid in the assignment of the peaks observed in the transmission IR experiments, we also examined the NO stretching frequency in each of the model complexes. To mitigate systematic errors in DFT-predicted stretching frequencies caused by both the harmonic approximation as well as the specific functional employed for the electronic structure calculations, we have shifted the calculated NO stretching frequencies ($\nu_{NO,DFT}$) by adding the difference between the frequency for gas phase NO evaluated at the same level of theory (2097 cm^{-1}) and the experimental value reported by NIST (1876 cm^{-1}) [53]. The resulting values ($\nu_{NO,est}$) are then directly comparable with the spectra obtained in the transmission IR experiments. This comparison is shown in Fig. 10, which juxtaposes our theoretical estimates for the maximum desorption temperatures (T_{max}) and NO stretching frequencies ($\nu_{NO,est}$) with the results of the IR-TPD experiments discussed in Section 3.2. Numerical values of the maximum desorption temperatures and calculated stretching frequencies are listed in Table S3 in the Supplemental Material. The results presented in Fig. 10 show that the TPD desorption feature centered at 430 K is due exclusively to NO adsorbed on Pd^{2+} cations at NNN Al pairs in the 6-rings. The vibrational frequency associated with this form of NO is predicted to be in the region of 1860 cm^{-1}. By contrast, the high-temperature NO desorption feature is due to NO adsorbed on Pd^{+} cations in a variety of environments. Between 550 and 750 K, NO will desorb from Pd^{+} cations at the NNN Al pairs in the 6-rings and the NNNNN Al pairs in the 8-rings. As a result, a decrease in IR intensity is expected in the range of the lower-frequency band (i.e., 1810 cm^{-1}). Finally, above 750 K, NO will desorb from Pd^{+} cations at NNN Al pairs in the 8-rings, resulting in the disappearance of the IR feature around 1860 cm^{-1}. Pd^{2+} cations at NNN Al pairs in the 8-rings might also provide very strong NO binding sites that contribute to both the high-temperature TPD feature and the 1860 cm^{-1} IR band.

Combined, our calculated desorption temperatures and IR stretching frequencies provide an interpretation that is consistent with the experimental observations from both TPD and IR TPD spectra. The main conclusion from this analysis is that the IR stretching frequencies for NO adsorbed on different Pd sites cover a broad frequency range and that NO adsorbed on Pd^{+} and Pd^{2+} contribute to the broad band observed in the region of 1860 cm^{-1}. This finding is consistent with that of Mandal et al. [25] who calculated frequencies of 1866 cm^{-1} and 1853 cm^{-1} for NO adsorbed on Pd^{2+} and Pd^{+} cations, respectively. They proposed that the band at 1810 cm^{-1} is likely due to the presence of NO adsorbed on partially hydrated Pd^{2+} cations [25]. However, our experimental conditions are different from those used by Mandal et al. who included both water and oxygen in the NO feed [25], and therefore their interpretation cannot explain our observations. Fig. 7 demonstrates that the band at 1810 cm^{-1} also appears in the IR spectrum when NO is adsorbed in the absence of water, on a Pd/H-CHA sample that was pretreated in dry air.

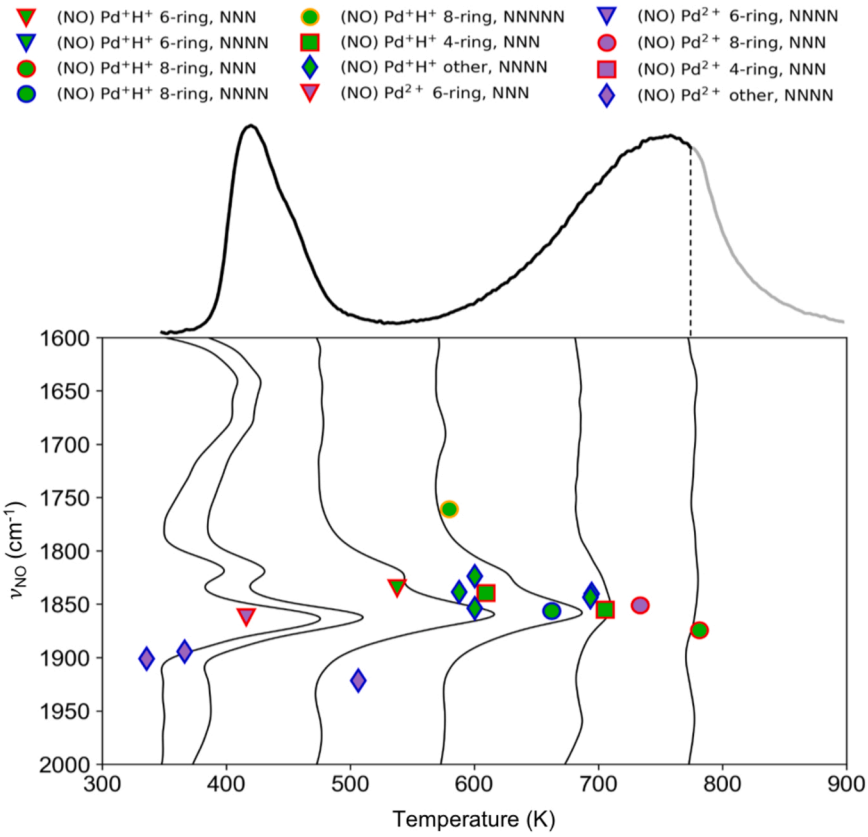

Fig. 10. Theoretical estimates of IR stretching frequencies for NO ($\nu_{NO,\ est}$) adsorbed on Pd^{+} and Pd^{2+} sites in Pd/H-CHA vs. calculated temperatures of maximum desorption (T_{max}) from the respective sites. Experimental IR spectra collected at 348 K, 373 K, 473 K, 573 K, 673 K and 773 K are shown as solid black lines. The corresponding TPD profile is shown above the graph. During TPD, the temperature was ramped from 348–773 K at 10 K/min and then held at 773 K for 20 min in He. The dashed line corresponds to the maximum temperature of 773 K; the TPD profile beyond this line represents the continued temporal evolution of the system at constant temperature.

Furthermore, Fig. 5 shows that exposure of adsorbed NO to water vapor has no effect on the band at 1810 cm^{-1}, but instead decreases the intensity of the band at 1860 cm^{-1}. We suggest that this lower frequency band is best attributed to NO adsorbed on $Pd^{+}H^{+}$ species at NNNN Al pairs in a 6-ring or at NNNNN Al pairs in an 8-ring, which have calculated frequencies of 1800 cm^{-1} and 1760 cm^{-1}, respectively.

It is also noteworthy that NO adsorption on the thermodynamically most favorable Pd^{2+} species at NNNN Al pairs in the 6-ring appears to be too weak to be relevant. The predicted maximum desorption temperature for these sites (270 K) is well below the temperature of the initial adsorption step (348 K). Nevertheless, it has been suggested that these sites might undergo partial reduction upon NO adsorption via the following reaction [15]:

$$Pd^{2+}(Z^{-})_2 + 2\ NO \rightarrow (NO)\ Pd^{+}\ Z^{-}\ NO^{+}\ Z^{-} \quad (3)$$

Our calculations show that reaction 3 is strongly exergonic, except for the highly stable Pd^{2+} sites at the NNNN pair in the 6-ring (for T = 348 K, P_{NO} = 20 Pa, ΔG_{rxn} = +26 kJ/mol). However, the experimental results presented here (see Fig. 6) show no evidence for the concurrent formation of $NO^{+}Z^{-}$ species when NO is adsorbed from He on Pd/H-CHA. Therefore, we conclude that reaction 3 is unlikely to occur. Furthermore, the experimentally observed NO storage capacity of Pd/H-CHA typically approaches a 1:1 ratio, 1 mol NO per mol of atomically dispersed Pd in the sample, indicating a low abundance of the thermodynamically most favorable Pd^{2+} sites at NNNN Al pairs in the 6-ring.

We have also calculated the thermodynamics for forming $NO^{+}Z^{-}$ on H-CHA via the reaction.

$$H{+}Z{-} + NO(g) + 0.25\ O_{2(g)} \rightarrow NO^{+}\ Z^{-} + 0.5\ H_2O_{(g)} \quad (4)$$

The formation of $NO^{+}Z^{-}$ is observed to occur on H-CHA (see Fig. 2), as evidenced by the appearance of the IR band at 2160 cm^{-1} and the concurrent consumption of zeolite protons and formation of adsorbed H_2O. Reaction 4 is predicted to have a free energy of reaction (ΔG^{0}_{rxn}) of − 12 kJ/mol for 200 ppm of NO (p_{NO} = 20 Pa) at 348 K, assuming only trace amounts of O_2 and H_2O (p_{O2} = p_{H2O} = 0.1 Pa) are present in the zeolite after the pretreatment. Our calculations predict an NO stretching frequency ($\nu_{NO,est}$) for $NO^{+}Z^{-}$ of 2073 cm^{-1}, consistent with the frequency range in which the IR band is observed in the experiments.

We have also considered the possibility that desorption occurs via the reaction.

$$NO^{+}Z^{-} + 0.5\ H_2O \rightarrow 0.5\ NO + 0.5\ NO_2 + H^{+}Z^{-} \quad (5)$$

Reaction 5 would explain how NO and NO_2 are formed in equivalent quantities, as can be seen in Fig. 3. Assuming only trace amounts of NO and NO_2 are present in the gas phase (p_{NO} = p_{NO2} = 0.1 Pa) at 348 K, ΔG^{0}_{rxn} = −28 kJ/mol if the water consumed in the desorption of $NO^{+}Z^{-}$ was retained on a Brønsted site, and ΔG^{0}_{rxn} = −18 kJ/mol if trace amounts of gas phase water (p_{H2O} = 0.1 Pa) are consumed instead. The results of our thermodynamic calculations for reactions 4 and 5 suggest that during the TPD, $NO^{+}Z^{-}$ is much more likely to desorb via reaction 5 than the reverse of reaction 4, consistent with the observation of significant amounts of NO_2 desorbing concurrently with NO.

3.5.2. *Effect of water on NO adsorption on Pd^{+} and Pd^{2+} sites*

To rationalize the effect of water vapor on NO adsorbed on Pd/H-CHA, we compare adsorption free energies for NO and water under typical conditions (200 ppm NO, 5% water, 348 K). These values are listed in Table 2 for a selection of Pd^{+} and Pd^{2+} sites. We find that water adsorbs strongly than NO on Pd^{2+} sites, but weakly on Pd^{+} sites. Therefore, a purge with He-containing water vapor after the NO adsorption step, as described in Section 3.3, is expected to displace NO from Pd^{2+} sites, but not from Pd^{+} sites. Our previous assignment of Pd^{2+} and Pd^{+} sites to the low-temperature and high-temperature TPD peaks, respectively, is therefore in agreement with the experimental observation that the low-temperature feature is missing in the TPD profile obtained after a wet purge. Similarly, the observation that the 1810 cm^{-1}

Table 2
Adsorption free energies (ΔG_{ads}) in kJ/mol for 200 ppm NO (P_{NO} = 20 Pa) and 5% water (P_{H2O} = 5 kPa) at 348.15 K on Pd^{2+} sites at NNN Al pairs, Pd^{+} and Pd^{2+} sites at NNN Al pairs in the 6-ring and 8-ring and Brønsted acid sites in CHA.

	$\Delta G_{ads,\ NO}$	$\Delta G_{ads,\ H2O}$
Pd^{+} $H^{+}(Z^{-})_2$		
NNN (6R)	-31	-8
NNNN (6R)	-40	-4
NNN (8R)	-79	-55
NNNN (8R)	-59	-34
NNNNN (8R)	-41	-44
$Pd^{2+}(Z^{-})_2$		
NNN (6R)	-9	-35
NNNN (6R)	+ 14	+ 33
NNN (8R)	-62	-113

feature in the IR spectrum is unaffected by the purge with He containing water vapor while the 1860 cm^{-1} feature is somewhat diminished in intensity agrees with our theoretical interpretation that the former is due to NO on Pd^{+} sites while the latter is due to a combination of NO on weak-binding Pd^{2+} and strong-binding Pd^{+} sites.

3.5.3. *Effects of O_2 on the adsorption of NO on Pd^{+} and Pd^{2+} sites*

As discussed in Section 3.4, when NO is adsorbed from air, the TPD profile exhibits strong peaks for NO and NO_2 centered at about 450 K and smaller, broader features around 575 K, but no high-temperature peak around 750 K. Using our theoretical analysis, in Section 3.5.1, we have attributed the low-temperature features to NO adsorbed on Pd^{2+} sites and the high-temperature features to NO adsorbed on Pd^{+} sites. Therefore, the experimental observations suggest that NO storage on Pd^{2+} sites increases, while NO storage on Pd^{+} sites decreases upon adsorption from air. This interpretation appears to be consistent with the phase diagrams shown in Fig. 9. These phase diagrams show that for NNN pairs in the 6-rings and 8-rings, Pd^{+} sites could be converted to Pd^{2+} sites under oxidizing conditions, with Pd^{2+} becoming more favorable relative to Pd^{+} at lower partial pressures of water. As argued above, the same is likely to be true for Al pairs in the 4-rings and those spanning adjacent rings for which the formation energy of Pd^{2+} is less than 50 kJ/mol higher than that of the corresponding Pd^{+} site at the same Al pair. Consequently, exposing Pd/H-CHA to air could result in an increased abundance of Pd^{2+} sites with maximum desorption temperatures below 500 K, formed by re-oxidation of Pd^{+} sites with maximum desorption temperatures between 500 and 750 K. As illustrated in Fig. 11, this change in the Pd speciation is consistent with the observed shift in the TPD profiles when NO is adsorbed from air instead of from He. Finally, Table S3 in the Supplemental Material shows that the IR signatures of NO adsorbed on the Pd^{+} sites that are lost in the re-oxidation process and those of NO adsorbed on the corresponding Pd^{2+} sites fall within the range of the broad peak at 1860 cm^{-1}, such that this interconversion of Pd sites may not be evident in the IR spectra.

4. Conclusions

In this study, we have investigated the adsorption of NO on H-CHA and Pd/H-CHA, and the effects of H_2O and O_2 on this process. NO adsorption on H-CHA involves a small percentage (~ 7%) of the Brønsted sites on the zeolite support and is characterized by an IR feature around 2160 cm^{-1}, and NO storage on the zeolite support is enhanced by the presence of O_2 and inhibited by the presence of water. Theoretical calculations of free energies support the interpretation of this adsorbed species as $NO^{+}Z^{-}$ and its formation being thermodynamically favorable. During TPD, this species can react with small amounts of adsorbed or free water to form NO and NO_2 in comparable amounts resulting in peaks centered at about 450 K. TPD profiles for NO adsorbed on Pd-CHA show two distinct desorption features, a low-temperature peak between 423 and 473 K and a broad high-temperature feature between 553 and 853 K which has a maximum at about 753 K. IR spectra of NO adsorbed on Pd/H-CHA exhibit two characteristic bands, around 1860 and 1810 cm^{-1}. The low-temperature desorption feature is eliminated in the presence of water, while the high-temperature feature is unaffected, while the opposite behavior is observed when NO is adsorbed in the presence of O_2. DFT calculations were used to determine the Gibbs free energies for NO adsorption on Pd^{+} and Pd^{2+} cations in different environments and the corresponding NO stretching

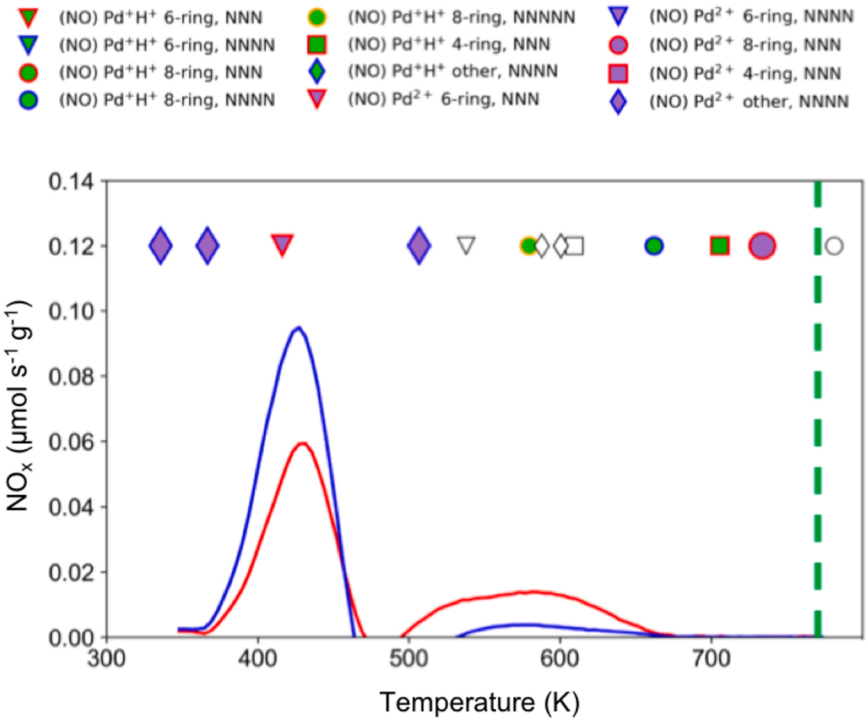

Fig. 11. Calculated temperatures of maximum desorption (T_{max}) from Pd^{+} and Pd^{2+} sites in Pd/H-CHA vs. corresponding experimental desorption profiles for NO (blue) and NO_2 (red) after NO adsorption from air. The blue and red curves in this graph represent the difference between the TPD profiles on Pd/H-CHA and H-CHA (see Fig. 7a and b) in order to isolate NO adsorption associated with the Pd sites. The dashed line corresponds to the maximum temperature of 773 K; the TPD profile beyond this line represents the continued temporal evolution of the system at constant temperature. The Pd^{+} sites that may be re-oxidized to Pd^{2+} sites by air exposure are represented by open symbols with black outlines. The corresponding Pd^{2+} sites at the same Al pairs, which may become more abundant by the oxidation of these Pd^{+} sites, are represented by enlarged symbols.

frequencies. We find that NO generally binds more strongly on Pd^{+} sites than on Pd^{2+} sites, suggesting that the former are responsible for the high-temperature desorption peak observed in the TPD experiments, while the latter contribute to the low-temperature feature. Calculated NO stretching frequencies reveal that the IR feature at 1810 cm^{-1} is due to NO adsorption on Pd^{+} sites with intermediate binding strength and a maximum-desorption temperature of about 550 K. The 1860 cm^{-1} feature contains contributions from both weakly-bound NO on Pd^{2+} sites desorbing below 500 K, and NO bound on Pd^{+} sites in different environments with peak desorption temperatures between 550 and 800 K. These findings show that the experimentally observed TPD and IR peaks cannot be assigned unambiguously to specific NO-Pd adsorption complexes. Taken in combination, the calculated desorption temperatures and IR stretching frequencies for NO adsorbed on Pd cations in different environments provide an interpretation that is consistent with the experimental observations from both TPD and IR spectroscopy. Our calculations also show that water can displace NO from Pd^{2+} sites, but not from Pd^{+} sites, corroborating the experimentally observed changes in the TPD and IR spectra upon exposure to water. These findings further support our interpretation of the underlying modes of NO adsorption.

CRediT authorship contribution statement

A. T, Bell and M. Head-Gordon – Conceived the project, P. Kim – Conducted the experimental work and its analysis, J. Van der Mynsburgge and H. Aljama – Carried out the theoretical calculations and their analysis, All authors were involved in writing and editing the manuscript.

Declaration of Competing Interest

The authors declare that they have no competing interests.

Acknowledgments

This material is based upon work supported by the U.S. Department of Energy's Office of Energy Efficiency and Renewable Energy (EERE) under the Vehicle Technologies Program Award Number DE-EE0008213. Additional support for computational modeling for JVdM, MHG and ATB was provided through the U.S. Department of Energy, Office of Science, Office of Advanced Scientific Computing Research and Office of Basic Energy Sciences, Scientific Discovery through Advanced Computing (SciDAC) program. Computational resources were also provided by UC Berkeley's Molecular Graphics and Computation Facility (supported by NIH S10OD023532). We also acknowledge useful discussions with our collaborators on this project at the University of Kentucky, Oak Ridge National Laboratory, Ford Motor Co., and BASF Chemical Company.

Disclaimer

Appendix A. Supporting information

Supplementary data associated with this article can be found in the online version at doi:10.1016/j.apcatb.2021.120992.

References

[1] Y. Ryou, J. Lee, S.J. Cho, H. Lee, C.H. Kim, D.H. Kim, Activation of Pd/SSZ-13 catalyst by hydrothermal aging treatment in passive NO adsorption performance at low temperature for cold start application, Appl. Catal. B Environ. 212 (2017) 140–149.
[2] T.A.C.a.E.C.A.T. Team, US DRIVE Advanced Combustion and Emission Control Roadmap, 2018.
[3] S.D. Burch, T.F. Potter, M.A. Keyser, M.J. Brady, K.F. Michaels, Reducing cold-start emissions by catalytic converter thermal management, SAE Trans. (1995) 348–353.
[4] B.-S. Kim, P.S. Kim, J. Bae, H. Jeong, C.H. Kim, H. Lee, Synergistic effect of Cu/CeO_2 and Pt–BaO/CeO_2 catalysts for a low-temperature lean NO_x trap, Environ. Sci. Technol. 53 (2019) 2900–2907.
[5] P. Khatri, D. Bhatia, Effect of gas composition on the NOx adsorption and reduction activity of a dual-function Ag/MgO/γ-Al_2O_3 catalyst, Appl. Catal. A Gen. 618 (2021), 118114.
[6] M. Moliner, A. Corma, From metal-supported oxides to well-defined metal site zeolites: the next generation of passive NO_x adsorbers for low-temperature control of emissions from diesel engines, React. Chem. Eng. 4 (2019) 223–234.
[7] Y. Ji, D. Xu, S. Bai, U. Graham, M. Crocker, B. Chen, C. Shi, D. Harris, D. Scapens, J. Darab, Pt-and Pd-promoted CeO_2–ZrO_2 for passive NOx adsorber applications, Ind. Eng. Chem. Res. 56 (2016) 111–125.
[8] W. Farneth, R. Gorte, Methods for characterizing zeolite acidity, Chem. Rev. 95 (1995) 615–635.
[9] F.-M. McKENNA, NOx trap composition, Google Patents, 2015.
[10] P. Sazama, L. Mokrzycki, B. Wichterlova, A. Vondrova, R. Pilar, J. Dedecek, S. Sklenak, E. Tabor, Unprecedented propane–SCR-NO_x activity over template-free synthesized Al-rich Co-BEA* zeolite, J. Catal. 332 (2015) 201–211.
[11] L.J. Lobree, A.W. Aylor, J.A. Reimer, A.T. Bell, NO Reduction by CH_4 in the Presence of O_2 over Pd-H-ZSM-5, J. Catal. 181 (1999) 189–204.
[12] Y. Zheng, L. Kovarik, M.H. Engelhard, Y. Wang, Y. Wang, F. Gao, Jn Szanyi, Low-temperature Pd/zeolite passive NO_x adsorbers: structure, performance, and adsorption chemistry, J. Phys. Chem. C 121 (2017) 15793–15803.
[13] Y. Ryou, J. Lee, H. Lee, C.H. Kim, D.H. Kim, Effect of various activation conditions on the low temperature NO adsorption performance of Pd/SSZ-13 passive NOx adsorber, Catal. Today 320 (2019) 175–180.
[14] K. Khivantsev, N.R. Jaegers, L. Kovarik, S. Prodinger, M.A. Derewinski, Y. Wang, F. Gao, J. Szanyi, Palladium/Beta zeolite passive NOx adsorbers (PNA): Clarification of PNA chemistry and the effects of CO and zeolite crystallite size on PNA performance, Appl. Catal. A Gen. 569 (2019) 141–148.
[15] K. Khivantsev, N.R. Jaegers, L. Kovarik, M. Wang, J.Z. Hu, Y. Wang, M. A. Derewinski, J. Szanyi, The superior hydrothermal stability of Pd/SSZ-39 in low temperature passive NOx adsorption (PNA) and methane combustion, Appl. Catal. B Environ. 280 (2021) 119449.
[16] Y. Cui, J. Zhu Chen, B. Peng, L. Kovarik, A. Devaraj, Z. Li, T. Ma, Y. Wang, J. Szanyi, J.T. Miller, Onset of high methane combustion rates over supported palladium catalysts: from isolated Pd cations to PdO nanoparticles, JACS Au 1 (2021) 396–408.
[17] B. Zhang, M. Shen, J. Wang, J. Wang, J. Wang, Investigation of various Pd species in Pd/BEA for cold start application, Catalysts 9 (2019) 247.
[18] R. Villamaina, U. Iacobone, I. Nova, E. Tronconi, M.P. Ruggeri, L. Mantarosie, J. Collier, D. Thompsett, Mechanistic insight in NO trapping on Pd/Chabazite systems for the low-temperature NOx removal from Diesel exhausts, Appl. Catal. B Environ. 284 (2021), 119724.
[19] A. Wang, K. Lindgren, M. Di, D. Bernin, P.-A. Carlsson, M. Thuvander, L. Olsson, Insight into hydrothermal aging effect on Pd sites over Pd/LTA and Pd/SSZ-13 as PNA and CO oxidation monolith catalysts, Appl. Catal. B Environ. 278 (2020), 119315.
[20] Y. Ryou, J. Lee, Y. Kim, S. Hwang, H. Lee, C.H. Kim, D.H. Kim, Effect of reduction treatments (H2 vs. CO) on the NO adsorption ability and the physicochemical properties of Pd/SSZ-13 passive NOx adsorber for cold start application, Appl. Catal. A Gen. 569 (2019) 28–34.
[21] K. Khivantsev, N.R. Jaegers, L. Kovarik, J.Z. Hu, F. Gao, Y. Wang, J. Szanyi, Palladium/zeolite low temperature passive NOx adsorbers (PNA): structure-adsorption property relationships for hydrothermally aged PNA materials, Emiss. Control Sci. Technol. (2019) 1–13.
[22] B. Pommier, P. Gelin, Infrared and volumetric study of NO adsorption on Pd-H-ZSM-5, Phys. Chem. Chem. Phys. 3 (2001) 1138–1143.
[23] K. Khivantsev, N.R. Jaegers, L. Kovarik, J.C. Hanson, F. Tao, Y. Tang, X. Zhang, I. Z. Koleva, H.A. Aleksandrov, G.N. Vayssilov, Achieving atomic dispersion of highly loaded transition metals in small-pore zeolite SSZ-13: high-capacity and high-efficiency low-temperature CO and passive NO_x adsorbers, Angew. Chem. 130 (2018) 16914–16919.
[24] K. Khivantsev, N.R. Jaegers, I.Z. Koleva, H.A. Aleksandrov, L. Kovarik, M. H. Engelhard, F. Gao, Y. Wang, G.N. Vayssilov, J. Szanyi, Stabilization of super electrophilic Pd^{+2} cations in small-pore SSZ-13 zeolite, J. Phys. Chem. C (2019) 309–321.

[25] K. Mandal, Y. Gu, K.S. Westendorff, S. Li, J.A. Pihl, L.C. Grabow, W.S. Epling, C. Paolucci, Condition-dependent Pd speciation and NO adsorption in Pd/zeolites, ACS Catal. (2020) 12801–12818.
[26] A. Gupta, S.B. Kang, M.P. Harold, NO_x uptake and release on Pd/SSZ-13: impact Of Feed composition and temperature, Catal. Today (2020).
[27] M. Ambast, A. Gupta, B.M.M. Rahman, L.C. Grabow, M.P. Harold, NO_x adsorption with CO and C2H4 on Pd/SSZ-13: experiments and modeling, Appl. Catal. B Environ. 286 (2021), 119871.
[28] C. Descorme, P. Gélin, M. Primet, C. Lécuyer, Infrared study of nitrogen monoxide adsorption on palladium ion-exchanged ZSM-5 catalysts, Catal. Lett. 41 (1996) 133–138.
[29] J. Van der Mynsbrugge, M. Head-Gordon, A.T. Bell, Computational modeling predicts the stability of both Pd^+ and Pd^{2+} ion-exchanged into H-CHA, J. Mater. Chem. A 2161–2174 (2020).
[30] H.-Y. Chen, J.E. Collier, D. Liu, L. Mantarosie, D. Durán-Martín, V. Novák, R. R. Rajaram, D. Thompsett, Low temperature NO storage of zeolite supported Pd for low temperature diesel engine emission control, Catal. Lett. 146 (2016) 1706–1711.
[31] S. Homeyer, W. Sachtler, Oxidative redispersion of palladium and formation of PdO particles in NaY: an application of high precision TPR, Appl. Catal. 54 (1989) 189–202.
[32] J. Jacquemin, S. Siffert, J.-F. Lamonier, E. Zhilinskaya, A. Aboukais, Catalytic properties of beta zeolite exchanged with Pd and Fe for toluene total oxidation. Studies in Surface Science and Catalysis, Elsevier, 2002, pp. 699–706.
[33] J.A. Loiland, R.F. Lobo, Oxidation of zeolite acid sites in NO/O_2 mixtures and the catalytic properties of the new site in NO oxidation, J. Catal. 325 (2015) 68–78.
[34] K. Hadjiivanov, J. Saussey, J. Freysz, J. Lavalley, FT-IR study of $NO+O_2$ co-adsorption on H-ZSM-5: re-assignment of the 2133 cm^{-1} band to NO+ species, Catal. Lett. 52 (1998) 103–108.
[35] T.M. Lardinois, J.S. Bates, H.H. Lippie, C.K. Russell, J.T. Miller, H.M. Meyer III, K. A. Unocic, V. Prikhodko, X. Wei, C.K. Lambert, Structural interconversion between agglomerated palladium domains and mononuclear Pd (II) cations in chabazite zeolites, Chem. Mater. 33 (2021) 1698–1713.
[36] Database of Zeolite Structures. ⟨http://www.iza-structure.org/databases/⟩.
[37] E. Mansoor, J. Van der Mynsbrugge, M. Head-Gordon, A.T. Bell, Impact of long-range electrostatic and dispersive interactions on theoretical predictions of adsorption and catalysis in zeolites, Catal. Today 312 (2018) 51–65.
[38] J.-D. Chai, M. Head-Gordon, Long-range corrected hybrid density functionals with damped atom–atom dispersion corrections, Phys. Chem. Chem. Phys. 10 (2008) 6615–6620.
[39] J.-D. Chai, M. Head-Gordon, Long-range corrected double-hybrid density functionals, J. Chem. Phys. 131 (2009), 174105.
[40] P.M. Zimmerman, M. Head-Gordon, A.T. Bell, Selection and validation of charge and Lennard-Jones parameters for QM/MM simulations of hydrocarbon interactions with zeolites, J. Chem. Theory Comput. 7 (2011) 1695–1703.
[41] Y.-P. Li, J. Gomes, S. Mallikarjun Sharada, A.T. Bell, M. Head-Gordon, Improved force-field parameters for QM/MM simulations of the energies of adsorption for molecules in zeolites and a free rotor correction to the rigid rotor harmonic oscillator model for adsorption enthalpies, J. Phys. Chem. C 119 (2015) 1840–1850.
[42] N. Mardirossian, M. Head-Gordon, Thirty years of density functional theory in computational chemistry: an overview and extensive assessment of 200 density functionals, Mol. Phys. 115 (2017) 2315–2372.
[43] T. Verstraelen, V. Van Speybroeck, M. Waroquier, ZEOBUILDER: A GUI Toolkit for the Construction of Complex Molecular Structures on the Nanoscale with Building Blocks, ACS Publications, 2008.
[44] Y. Shao, Z. Gan, E. Epifanovsky, A.T. Gilbert, M. Wormit, J. Kussmann, A.W. Lange, A. Behn, J. Deng, X. Feng, Advances in molecular quantum chemistry contained in the Q-Chem 4 program package, Mol. Phys. 113 (2015) 184–215.
[45] S. Grimme, Supramolecular binding thermodynamics by dispersion-corrected density functional theory, Chem. Eur. J. 18 (2012) 9955–9964.
[46] S. Yasumura, C. Liu, T. Toyao, Z. Maeno, K.-I. Shimizu, Lean NO_x capture and reduction by NH_3 via NO^+ intermediates over H-CHA at room temperature, J. Phys. Chem. C. 125 (2021) 1913–1922.
[47] S. Bordiga, L. Regli, C. Lamberti, A. Zecchina, M. Bjørgen, K.P. Lillerud, FTIR adsorption studies of H_2O and CH_3OH in the isostructural H-SSZ-13 and H-SAPO-34: formation of H-bonded adducts and protonated clusters, J. Phys. Chem. B 109 (2005) 7724–7732.
[48] C. Sedlmair, B. Gil, K. Seshan, A. Jentys, J.A. Lercher, An in situ IR study of the NO_x adsorption/reduction mechanism on modified Y zeolites, Phys. Chem. Chem. Phys. 5 (2003) 1897–1905.
[49] F. Lónyi, H.E. Solt, J. Valyon, H. Decolatti, L.B. Gutierrez, E. Miró, An operando DRIFTS study of the active sites and the active intermediates of the NO-SCR reaction by methane over In, H-and In, Pd, H-zeolite catalysts, Appl. Catal. B Environ. 100 (2010) 133–142.
[50] A. Kvasničková, P. Kočí, Y. Ji, M. Crocker, Effective model of NO_x adsorption and desorption on $PtPd/CeO_2$-ZrO_2 passive NO x adsorber, Catal. Lett. 150 (2020) 3223–3233.
[51] K.I. Hadjiivanov, Identification of neutral and charged N_xO_y surface species by IR spectroscopy, Catal. Rev. 42 (2000) 71–144.
[52] H. Aljama, M. Head-Gordon, A.T. Bell, Assessing the stability of Pd-exchanged sites in zeolites with the aid of a high throughput quantum chemistry workflow, Res. Sq. (2021), https://doi.org/10.21203/rs.3.rs-396201/v1.
[53] NIST Chemistry WebBook. ⟨https://webbook.nist.gov/⟩.